Combining Desferriferrioxamine B and 1-Hydroxy-2-Piperidone ((PIPO)H) to Chelate Zirconium. Solution Structure of a Model Complex of the [89 Zr]Zr–DFOcyclo*–mAb Radioimmunoconjugate

Floriane Mangin, Osian Fonquernie, Pawel Jewula, Stéphane Brandès, Marie-josé Penouilh, Quentin Bonnin, Bruno Vincent, Enrique Espinosa, Emmanuel Aubert, Michel Meyer, et al.

ChemPlusChem

Research Article
doi.org/10.1002/cplu.202400062

Chemistry Europe
European Chemical Societies Publishing

www.chempluschem.org

Combining Desferriferrioxamine B and 1-Hydroxy-2-Piperidone ((PIPO)H) to Chelate Zirconium. Solution Structure of a Model Complex of the [^{89}Zr]Zr–DFOcyclo*–mAb Radioimmunoconjugate

Floriane Mangin,[a] Osian Fonquernie,[a] Pawel Jewula,[a] Stéphane Brandès,[a] Marie-José Penouilh,[a] Quentin Bonnin,[a] Bruno Vincent,[b] Enrique Espinosa,[c] Emmanuel Aubert,*[c] Michel Meyer,*[a] and Jean-Claude Chambron*[a, b]

^{89}Zr–immunoPET is a hot topic as ^{89}Zr cumulates the advantages of ^{64}Cu and ^{124}I without their drawbacks. We report the synthesis of a model ligand of a chiral bioconjugable tetrahydroxamic chelator combining the desferriferrioxamine B siderophore and 1-hydroxy-2-piperidone ((PIPO)H), a chiral cyclic hydroxamic acid derivative, and the study by NMR spectroscopy of its zirconium complex. Nuclear Overhauser effect measurements (ROESY) indicated that the complex exists in the form of two diastereomers, in 77 : 23 ratio, resulting from the combination of the central chiralities at the 3-C of the (PIPO)H component and at the Zr^{4+} cation. The 44 lowest energy structures out of more than 1000 configurations/conformations returned by calculations based on density functional theory were examined. Comparison of the ROESY data and the calculated interatomic H···H distances allowed us to select the most probable configuration and conformations of the major complex.

Introduction

The development of ^{89}Zr as radioisotope in targeted positron emission tomography (PET) is relatively recent,[1] although the production of ^{89}Zr and its use for labeling a monoclonal antibody (mAb) *via* chelation to a DTPA (diethylenetriamine pentaacetic acid) derivative was reported as early as 1986.[2] The interest of this radionuclide in investigations by immunoPET over ^{64}Cu, ^{86}Y, and ^{124}I stems from various factors. ^{89}Zr has a half-life of 78.4 h, shorter than ^{124}I (100.3 h), but much longer than *ca.* 12 h for ^{64}Cu and ^{86}Y. As a matter of fact, the slightly longer than 3 days half-life is commensurable with the slow kinetics of antibody accumulation at the surface of tumor cells in order to obtain optimal tumor-to-nontumor ratios. In addition, ^{89}Zr decays through the emission of a positron of relatively low mean energy (395.5 keV) by comparison with ^{124}I (687 and 974 keV). As a consequence, the intrinsic spatial resolution loss in using ^{89}Zr (1 mm) is only slightly less than ^{64}Cu (0.7 mm), but better than ^{86}Y and ^{124}I (1.8 and 2.3 mm, respectively).[1a,d] Therefore, ^{89}Zr represents a good compromise among ^{64}Cu, ^{86}Y, and ^{124}I. Another advantage of ^{89}Zr over ^{124}I is that it is produced directly from a 100% natural abundance isotope (^{89}Y), which is not the case for ^{124}I. Comprehensive procedures for the production of ^{89}Zr–mAbs were published in 2003,[3] and were followed a few years later by the first clinical tests using a ^{89}Zr-labelled mAb.[4]

Desferriferrioxamine B ($(DFO)H_3$; represented as mesylate salt $[(DFO)H_4](CH_3SO_3)$ in Figure 1), is a natural iron chelator incorporating in its linear backbone three acyclic –N(OH)C(O)– hydroxamic acid functions, which have the same orientation and are separated from each other by $-(CH_2)_2C(O)NH(CH_2)_5-$ sequences.[5] $[(DFO)H]^{2-}$ forms a very stable complex with Fe^{3+} (log $K_f = 30.6$),[6] in which the three hydroxamate chelate subunits occupy three edges of the coordination octahedron of the metal cation in the *N-cis,cis* configuration.[7] Noteworthy, $[(DFO)H_4](CH_3SO_3)$ is prescribed under the registered trademark Desferal® to patients suffering from iron overload. In addition, since the work of Herscheid and coworkers,[8] $(DFO)H_3$ has been employed as the standard chelator for the development of ^{89}Zr-based radioimmunoconjugates, because of (i) its commercial availability and (ii) the presence of the terminal amine function, which can be used for attaching suitable spacers and reactive groups for bioconjugation.[9]

[a] Dr. F. Mangin, Dr. O. Fonquernie, Dr. P. Jewula, Dr. S. Brandès, M.-J. Penouilh, Dr. Q. Bonnin, Dr. M. Meyer, Dr. J.-C. Chambron
Institut de Chimie Moléculaire de l'Université de Bourgogne
UMR 6302 CNRS, Université de Bourgogne
9, avenue Alain Savary, BP 47870, 21078 Dijon Cedex, France
E-mail: michel.meyer@u-bourgogne.fr

[b] Dr. B. Vincent, Dr. J.-C. Chambron
Institut de Chimie de Strasbourg
UMR 7177 CNRS, Université de Strasbourg
4, rue Blaise Pascal, 67070 Strasbourg, France
E-mail: jcchambron@unistra.fr

[c] Prof. Dr. E. Espinosa, Dr. E. Aubert
Université de Lorraine
CNRS, CRM2
54000 Nancy, France
E-mail: emmanuel.aubert@univ-lorraine.fr

Supporting information for this article is available on the WWW under https://doi.org/10.1002/cplu.202400062

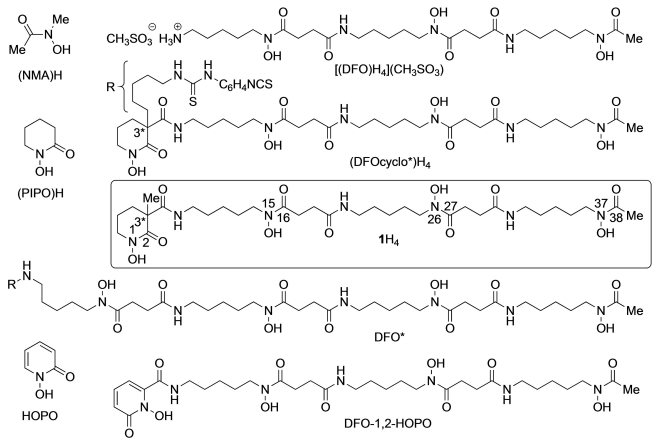

Figure 1. Chemical structures of the DFO-derived chelators mentioned in this study, including the title compound $\mathbf{1}H_4$, and subcomponent hydroxamic acids. Numbered atom labels in $\mathbf{1}H_4$ are those of the oxygen atoms of the hydroxamic acid moieties. 3* marks the asymmetric centers of $\mathbf{1}H_4$ and (DFOcyclo*)H_4.

Zirconium is the second row group IV metal. It achieves the stable d^0 configuration as a hard Lewis acidic Zr^{4+} cation, which forms coordination complexes with anionic oxygen donors. Its relatively large ionic radius of 0.84 Å favors a coordination number as high as 8. As Zr^{4+} has no crystal-field stabilization energy, its preferred coordination geometry is the square antiprism. Therefore, DFO^{3-} is far from being the ideal zirconium chelator, because this hexadentate trishydroxamate binder alone cannot fulfill the coordination sphere of Zr^{4+}. The assistance of auxiliary ligands is thus needed. As a matter of fact, the Zr^{4+} complex prevailing at physiological pH is usually formulated as an eight-coordinated species, the two remaining coordinating sites being most likely occupied by monodentate hydroxo anions and/or water molecules,[10] DFT calculations indicating that $[Zr(DFO)(OH)_2]$ was the most energetically favorable species.[10c] Therefore, the stability of the zirconium complex would be increased by replacing the hydroxo anions and/or water molecules by a chelating unit incorporating anionic oxygen donor atoms, such as those found in catecholate (dianionic) or hydroxamate (singly-anionic) ligands. This observation has led to the development of a diversity of hydroxamate-based Zr chelators, in particular deriving from $(DFO)H_3$, with more than three bidentate ligand subunits.[11] It must be noted that the idea of the extension of $(DFO)H_3$ with a fourth chelating unit, as a means to create a chelator for tetravalent metal cations such as Pu^{4+}, dates back to the pioneering works of Raymond and coworkers.[12] By taking advantage of the primary amine function of $(DFO)H_3$ for anchoring a fourth binding unit to the siderophore by amide bond formation, they could obtain DFOs extended with either 1,2-catechol in DFOCAM(C) and DFOMTA,[12a] or 1,2-hydroxypyridone in DFO-1,2-HOPO.[12b] For example, the formation constants (log K_f) of the Th^{4+} and Pu^{4+} complexes increased by 6–7 order of magnitude from 26.6 to 33.7 and 30.8 to 36.9, respectively, upon substitution of DFO for DFO-1,2-HOPO.[13]

The improved stability in the serum of the Zr^{4+} complex of DFO-1,2-HOPO itself by comparison with DFO was recently disclosed.[11h] However, as early as in 2014, Mindt and coworkers had homologated DFO into the tetrahydroxamate chelator DFO*,[11c] which was subsequently conjugated to the trastuzumab monoclonal antibody (mAb) using the *p*-phenylenediisothiocyanate (PDTCI) strategy. The [^{89}Zr]Zr–DFO*–trastuzumab radiotracer showed a significantly lower uptake in bone containing organs than the DFO-based radiotracer.[11i] Alternatively, Rudd *et al.* used the squaramide ester as an electrophile for bioconjugation of DFO by reaction with lysine side chains.[11q] As in EDTA competition experiments, the [^{89}Zr]Zr complex of a water soluble DFO squaramide ester model released significantly less zirconium than a DFO analogue, the authors concluded that their chelator was actually a tetrachelate, the *cis*-dicarbonyl moiety of the squaramide forming the fourth chelate ring. More recently, Price and coworkers, reported that the stability of [^{89}Zr]Zr–(DFO–Km)–IgG, a radioimmunoconjugate based on an extended DFO incorporating a lysine, was significantly greater in vivo than its DFO analogue.[11u]

A crucial point in the design of chelators is their capacity to fulfill the coordination demands of the metal cation. If there exists no example of structures of Zr^{4+} complexes with extended DFOs neither in solution (NMR spectroscopy), nor in the solid state (X-ray diffraction), DFT calculations have been performed successfully on Zr(IV) complexes with various chelators.[11c,m,s,u,14]

We recently reported on a new bioconjugable Zr^{4+} chelator, (DFOcyclo*)H_4 (Figure 1), which was obtained by extension of $(DFO)H_3$ with a cyclic hydroxamic acid derived from the 6-membered heterocycle 1-hydroxy-2-piperidone, denoted (PIPO)H.[15,16] This fragment[17] is found as a terminal chelating unit in a number of siderophores (e.g., exochelin MN,[18a] tsukubachelin,[18b] and albisporachelin,[18c] just to mention a few). Contrary to *N*-methylacetohydroxamate NMA^-, a model of the linear hydroxamate fragments found in DFO^{3-}, which we demonstrated to exist mainly in the *trans* or *E* form,[19] $PIPO^-$ is preorganized for chelation, as the oxygen donor atoms are in the *cis* configuration by construction. Therefore, we envisioned that the extension of $(DFO)H_3$ with (PIPO)H would confer improved binding properties towards tetravalent metals to the resulting chelator, in particular Zr^{4+}, as this cation would be surrounded by four hydroxamate chelate rings, including a preorganized one. We provided evidence of the increased stability of the [^{89}Zr]Zr complex of (DFOcyclo*)H_4 by comparison with the [^{89}Zr]Zr complex of $(DFO)H_3$ using *in vitro* and *in vivo* experiments.[15a] In particular, *in vivo* biodistribution experiments performed on $HER2^+$ SKOV-3 and $HER2^-$ MDA-MB-231 tumor-bearing mice showed that the injected dose (ID) of radioactivity per gram of bones a week after injection was for the DFOcyclo*-based bioconjugate at least twice as less as for the DFO-based bioconjugate. By contrast, the radioactivity uptake by the tumor was systematically higher in the case of the latter, 93 *vs.* 72% ID/g for $HER2^+$ SKOV-3, and 20 *vs.* 16% ID/g for $HER2^-$ MDA-MB-231.

It is important to note that (DFOcyclo*)H_4 is chiral because it contains an asymmetric center, the carbon atom 3-C of the (PIPO)H chelate that bears the DFO component and the arm functionalized for bioconjugation (substituent R in Figure 1). Besides, any particular winding of the chelator around the zirconium cation generates a chiral-at-metal complex. As a consequence, the combination of the chirality at 3-C and the chirality at the metal should generate at minimum two diastereomeric complexes.[20] Ideally, it is highly desirable that the diastereomeric ratio (*d.r.*) is as close as possible to 1:0, which means that the chirality at 3-C strictly controls the chirality at the metal. Such a control was observed in the Zr tetrahydroxamate complex of a DFO derivative incorporating a glutamic-acid moiety.[11s] In order to investigate this important issue, we synthesized **1**H_4 (Figure 1), a simple tetrahydroxamic acid analogue of (DFOcyclo*)H_4, in which the original R substituent has been replaced by a simple methyl group. This model chelator has been subsequently used for the preparation of the Zr(IV) complex [Zr(**1**)], the solution structure of which has been investigated by comparison of the results of extensive NMR studies (^{1}H, ^{13}C, ^{15}N, and the corresponding homo- and heteronuclear correlations) with the structures obtained by DFT calculations.

Results and Discussion

Synthesis of 1H_4 and of Models of the (PIPO)H Fragment, and their Zr^{4+} Complexes

1H_4 was prepared in four steps from the known benzyl-protected cyclic hydroxamic acid **3**, the 3-C carbon atom of which is substituted by an ethylcarboxylate ester function (Schemes 1 and 3).[21] As a consequence, this carbon is asymmetric. However, its location between the ester and hydroxamate carbonyl functions makes the corresponding 3-H proton acidic, and the compound prone to "keto-enol" tautomerism. In fact, the nucleophilic character of 3-C in basic conditions was used to anchor the pendant functionalized pentamethylene chain of (DFOcyclo*)H_4 used for coupling of the chelator to an antibody. For the model *rac*-**1**H_4, 3-C was substituted with a simple methyl group, which allowed us to have at our disposal a stereochemically stable (PIPO)H precursor.

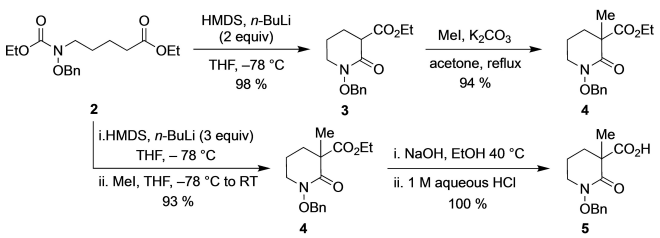

Scheme 1. (Top) two-step preparation of the benzyl protected (PIPO)H precursor **4** and (bottom) one-pot procedure followed by saponification and acidification to **5**.

As shown in Scheme 1, **3** was reacted first with an excess of methyl iodide in acetone at reflux for 3 days using potassium carbonate as base to afford its methylated analogue **4** in 94% yield. Alternatively, compound **4** can be prepared in a one pot reaction from diester **2**, which is the direct precursor of **3**. As reported, cyclization of **2** into **3** was performed by using LiHMDS generated *in situ* as base. However, in order to generate the lithium malonate-like tautomer of **3** *in situ*, one more equivalent of LiHMDS had been introduced in the reaction mixture. The latter was finally quenched with methyl iodide, which afforded compound **4** in 93% yield after chromatographic purification. Saponification of ethylester **4** was performed by reaction with sodium hydroxide in ethanol and afforded 3-methyl-1-benzyloxy-2-oxopiperidinecarboxylic acid (**5**) in quantitative yield.

Next, the conditions of the coupling reaction between (DFO)H_3 and **5** were set up first by using 1-octylamine as (DFO)H_3 model. A number of reagents, auxiliaries, and bases have been used for amide bond formation by direct coupling of a carboxylic acid and an amine. We chose the classical combination of *N*-ethyl-*N*′-(3-dimethylaminopropyl)carbodiimide hydrochloride (EDC·HCl) as coupling reagent, HOBt as additive, and diisopropylethylamine as base (Scheme 2, entry 1), which had been already successfully used for the coupling of carboxylic acids to (DFO)H_3.[22] The reaction was first run at room temperature in dimethylformamide. After 6 days, the temperature was increased to 40 °C and the reaction conducted for a further 4 days. In these conditions, compound **6** was obtained in 75% yield after purification by chromatography. We therefore used these reaction conditions for the direct coupling of **5** and [(DFO)H_4](CH_3SO_3). The DFO conjugate **7** was obtained in 79% isolated yield after 4 days reaction at 40 °C and purification of the neutralized reaction mixture on a C-18 reverse-phase flash chromatography column using H_2O/CH_3CN as eluent (Scheme 3).

The hydroxamic acid benzyl-protecting group of **6** could be conveniently removed by Pd-catalyzed hydrogenolysis under 1 atm of dihydrogen using 10% Pd/C. These conditions worked equally well for the hydrogenolysis of the conjugate **7**, affording the chelator **1**H_4 in 95% yield in pure form after precipitation from methanol/acetone (Schemes 2 and 3).

N-Methyl 3-methyl-1-hydroxy-2-oxo-3-piperidinecarboxamide (**10**H) was considered as a more reliable model of the (PIPO)H fragment in **1**H_4 than (PIPO)H itself, because it carries a methyl carboxamide function at the 3-C position, as a mimic of the amide bridge in chelator **1**H_4 (Scheme 2, entry 2). It was prepared in two steps from **5**, by reaction with the

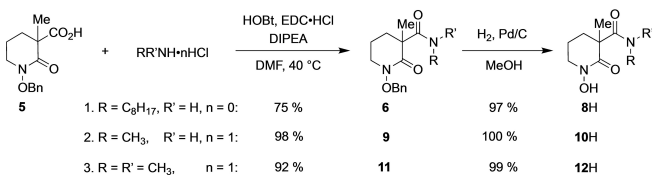

Scheme 2. Preparation of model carboxamide-substituted (PIPO)H compounds (entries 1–3).

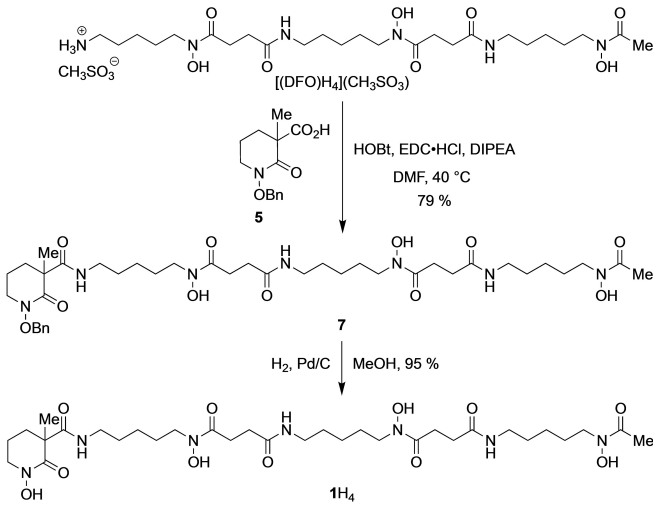

Scheme 3. Synthesis of *rac*-$\mathbf{1}H_4$ from $[(DFO)H_4](CH_3SO_3)$ and compound **5** followed by hydrogenolysis.

hydrochloride salt of methylamine in the same conditions as reported for the preparation of compounds **6** and **7** to afford intermediate **9** in 98% yield, which was deprotected quantitatively by Pd/C-catalyzed hydrogenolysis. We also used these reaction conditions for the synthesis of *N*,*N*-dimethyl 3-methyl-1-hydroxy-2-oxo-3-piperidinecarboxamide (**12**H) (Scheme 2, entry 3). Reaction of **5** with the hydrochloride salt of dimethylamine afforded intermediate **11** in 92% yield, which was deprotected by hydrogenolysis to afford compound **12**H in 99% yield.

The Zr^{4+} complex of chelator $\mathbf{1}H_4$, as well as those of the model ligand **10**H were prepared by reacting stoichiometric amounts of $[Zr(acac)_4]$ with each ligand. They were obtained in reasonably pure form after solvent removal, dissolution in methanol, and precipitation by the addition of acetone as counter solvent. The LC-MS of the complex [Zr(**1**)] (HPLC traces and corresponding ESI mass spectrum) are reproduced in Figures S51–S53). The study of $[Zr(\mathbf{10})_4]$ by ^{1}H NMR is summarized in the Supporting Information (p. S10 and Figure S54). The next section focusses on the NMR spectroscopy studies of $\mathbf{1}H_4$ and its Zr^{4+} complex, [Zr(**1**)].

NMR Spectroscopy Studies

Atom labelling of the chelator $\mathbf{1}H_4$ is displayed in the inserts of Figures 2b and 3a. The pentamethylene and ethylene chains interconnecting the amide and hydroxamic functions are identified as $C_5(1)$, $C_2(1)$, $C_5(2)$, $C_2(2)$, and $C_5(3)$ starting from the side of the (PIPO)H component. The ^{1}H NMR spectrum of the

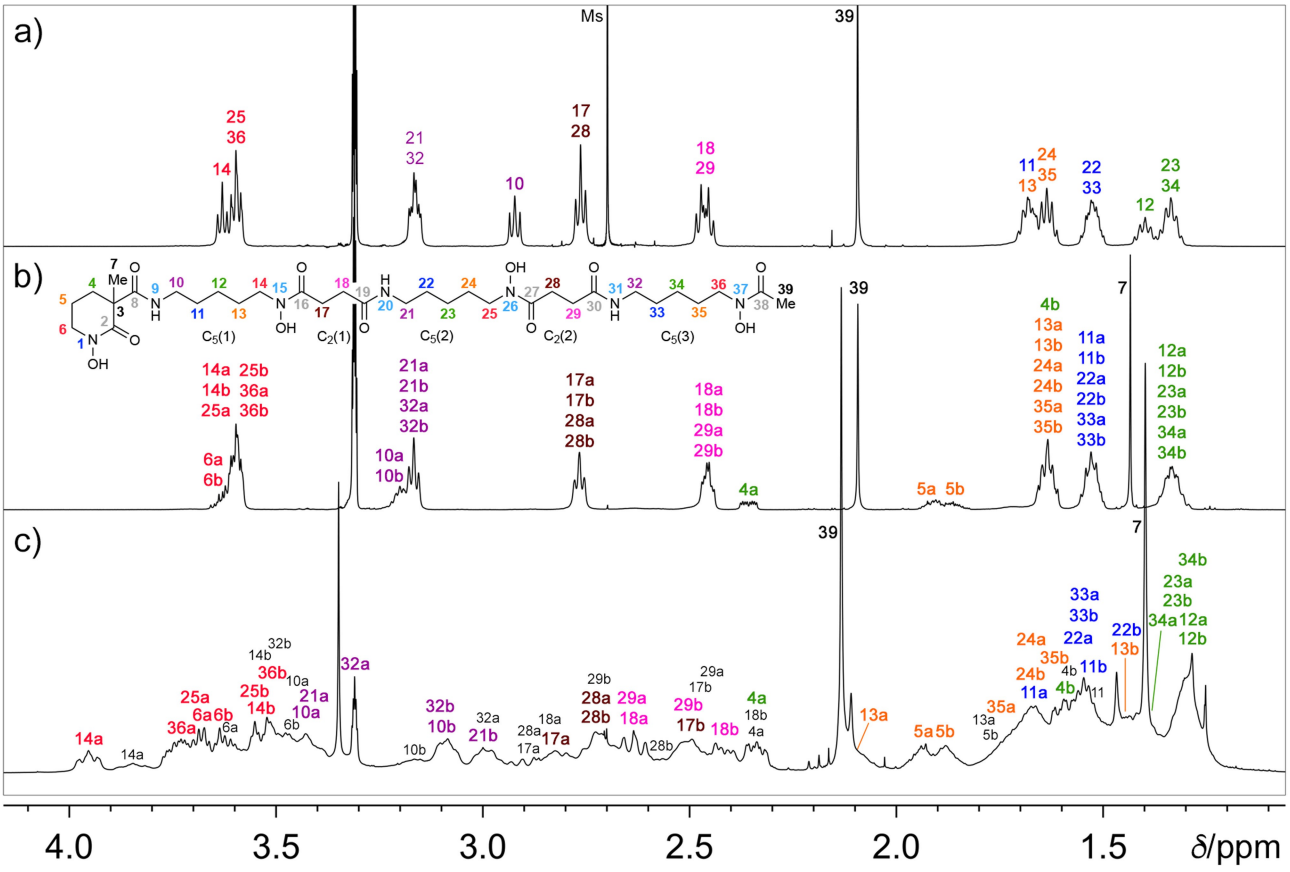

Figure 2. Stacked plots of the ^{1}H NMR spectra of (a) $[(DFO)H_4](CH_3SO_3)$, (b) $\mathbf{1}H_4$ (600.23 MHz, CD_3OD, 300 K), and (c) [Zr(**1**)] (500.13 MHz, CD_3OD, 295 K). The labels a and b of the major diastereomer of [Zr(**1**)] refer to deshielded and shielded signals in a given geminal pair of protons. Proton labels of the minor diastereomer that could be identified with certainty are shown in light grey.

chelator $\mathbf{1}H_4$ is displayed in Figure 2b together with those of $[(DFO)H_4](CH_3SO_3)$ (Figure 2a) and [Zr(**1**)] (Figure 2c) for comparison. The ^1H, ^{13}C, and ^{15}N chemical shift data of these compounds are collected in Tables S1 and S2. The ^1H NMR spectra of $[(DFO)H_4](CH_3SO_3)$ and $\mathbf{1}H_4$ differ by the signature of the (PIPO)H subunit in the latter, with its characteristic multiplet for the signal of 4a-H at 2.357 ppm. The signals of protons 10-H are shifted downfield in $\mathbf{1}H_4$, in the region of the signals of their homologues 21-H and 32-H because of their proximity to an amide nitrogen atom. Otherwise, protons 11-H to 14-H, 21-H to 25-H, and 32-H to 36-H of $\mathbf{1}H_4$ show slight differences of chemical shifts by comparison with those of $[(DFO)H_4]^+$. The same is true for 18-H and 29-H. It must be noted that the signals of the amide protons of $\mathbf{1}H_4$ show up at 7.644 ppm for 9-H, and 7.920 ppm for 20-H and 31-H. In the ^{13}C NMR spectrum (Figure S46), the signals of the hydroxamic carbonyl carbon atoms 16-C, 27-C, and 38-C, and of the amide carbonyl carbon atoms 19-C and 30-C of the DFO component, and the signal of the amide carbonyl connecting the PIPO subunit to the DFO component (8-C) are located in the same narrow chemical shift range (173.5–174.9 ppm), as for the corresponding $[(DFO)H_4]^+$ carbonyl carbon atoms, whereas 2-C, the hydroxamic carbonyl carbon atom of the PIPO component, resonates upfield (169.2 ppm).

$^{15}N/^1H$ HMBC experiments (Figure S49) gave different fingerprints for the hydroxamic and the amide nitrogen atoms. The hydroxamic nitrogen atom 1-N of the PIPO component resonates in the same region as those of the DFO component (15-N, 26-N, and 37-N), *i.e.* around −203 ppm. By comparison, the signals of the amide nitrogen atoms are shifted upfield, and appear at −265 (9-N) and −260 ppm (20-N and 31-N).

As shown in Figure 2c and S61, the ^1H NMR spectrum of [Zr(**1**)] shows broad features and multiple overlaps by comparison with the spectrum of $\mathbf{1}H_4$. Similar broadening had been noted in the cases of a model complex of [Zr(DFO*)][11c] and the complex [Zr(DFO–Km)].[11u] Whereas the assignment of the spectrum of $\mathbf{1}H_4$ was straightforward, as it is more-or-less the superposition of the spectra of $[(DFO)H_4](CH_3SO_3)$ and of (PIPO)H, the assignment of the spectrum of its Zr^{4+} complex required the use of 2D NMR experiments such as $^1H/^1H$ COSY, ROESY, and pure-shift TOCSY, pure-shift $^{13}C/^1H$ HSQC, $^{13}C/^1H$ H2BC, $^{13}C/^1H$ HMBC, and $^{15}N/^1H$ HMBC. In order not to make the present text cumbersome, the sequence of steps, which allowed us to assign the signals of all the proton, carbon, and nitrogen atoms of [Zr(**1**)], are presented in the Supporting information (pp. S10–S13). We show, as an illustration, the combined pure-shift $^{13}C/^1H$ HSQC and $^1H/^1H$ ROESY maps of the complex in Figure 3.

It is important to mention that in the ROESY map of Figure S55, the presence of correlation spots displaying the same phase as the diagonal (*i.e.*, TOCSY spots) indicated that at least two species were in exchange in solution. Noticeably, the signal of 14a-H displays an exchange correlation spot with a similar, but lower intensity signal at 3.85 ppm, which can therefore be attributed to a 14-H proton of the minor species. Integration of these signals gives an intensity ratio of *ca.* 77:23 between the major and the minor species (Figure S61). By contrast, the ^{13}C NMR spectrum of [Zr(**1**)] (Figure S68) showed reasonably sharp signals forming a major set together with a set of minor signals.

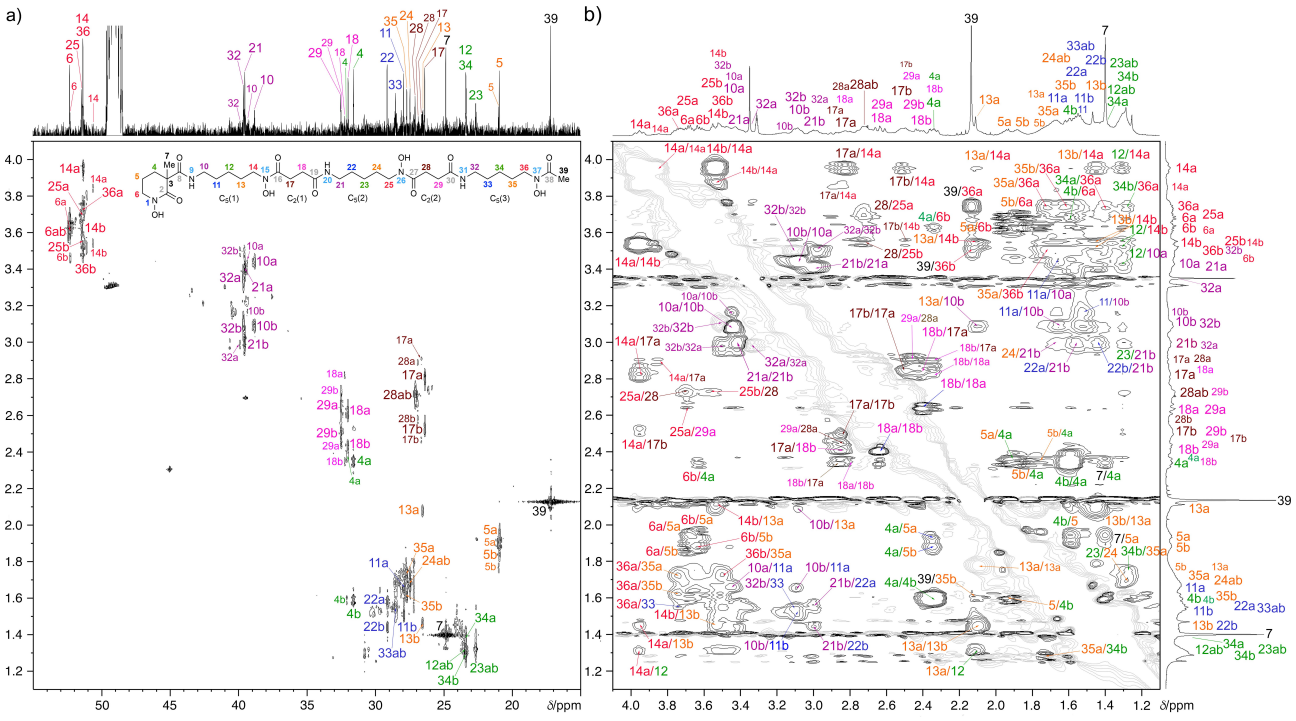

Figure 3. (a) Pure-shift $^{13}C/^1H$ HSQC (500.24 MHz, CD_3OD, 298 K) and (b) $^1H/^1H$ ROESY (500.13 MHz, CD_3OD, 295 K) maps of the major diastereomer of [Zr(**1**)] in methanol solution. In the ROESY map, the correlation spots are in black and the exchange spots are in light grey, as the diagonal.

The ^{1}H NMR spectrum of [Zr(**1**)] studied and described so far had been recorded at 295 K in CD_3OD. VT ^{1}H NMR between 260 and 335 K showed the following features (Figure S66): At 335 K all the signals were broad, those of 4a-H and 4b-H excepted, the former appearing as a clear eight-line (2-4-2) multiplet above 325 K and the latter as a seven-line (2-3-2) multiplet above 295 K. At 260 K, the spectrum showed even broader features than at 335 K, but transient signal sharpening was noted for the resonances of protons 6-H and 14-H at 295 K. Comparison of the ^{13}C NMR spectra at 300 and 193 K showed that the signals of the carbonyl carbon atoms were not affected by the temperature variation.

The ^{1}H and ^{13}C NMR spectra of **1**H_4 and [Zr(**1**)] being fully assigned, it was interesting to compare the variations of the chemical shifts of analogous protons upon going from the free chelator to its zirconium complex (Figure 2 and Table S2). The positions of the signals of the PIPO component are left more-or-less unchanged (4a-H, 5b-H, 6b-H) or shifted downfield (more significantly for 4b-H by comparison with 5a-H and 6a-H), or upfield (7-H). The signals of the DFO component are also affected by the complexation. In the free ligand, protons in similar topological chemical environments, hence marked with identical colors, give overlapping signals. Such is the case of the protons belonging to the triads {10-H, 21-H, 32-H} in purple, {11-H, 22-H, 33-H} in blue, {13-H, 24-H, 35-H} in orange, and {14-H, 25-H, 36-H} in red, and the diads {17-H, 28-H} in brown, and {18-H, 29-H} in pink. Upon complexation, the signals of the protons belonging to a same diad or triad are scattered. This indicates that the anisotropy of the environments of the geminal protons of a methylene group, which are diastereotopic in the free ligand as well as in the complex, is enhanced by complexation. This is not surprising as, in the complex, the chelator takes up a curled conformation (see next section), which generates a second stereogenic element, the central chirality at Zr^{4+}. Contrary to the chirality at 3-C, the latter affects the diastereotopic protons whatever their location along the backbone of the DFO component. In general (Table S2), the values of the $\Delta\delta$ of complexation are usually between -0.100 and 0.100 ppm, except for the signals of protons 10b-H (-0.115), 10a-H (0.241), 21a-H (0.248), and 32a-H (0.166); 11a-H (0.127); 13a-H (0.454) and 13b-H (-0.190); 17b-H (-0.251); 18a-H and 29a-H (0.180); 14a-H (0.356) and 36a-H (0.149) (underlined are the signals exhibiting the largest complexation-induced shifts, CIS). Other signals showing large CIS values are those of the amide protons 9-H and 31-H, and, to a lesser extent, 20-H, which are shifted downfield by 0.388, 0.255, and 0.112 ppm, respectively. These observations will be discussed in the light of the formation of intramolecular hydrogen bonds upon complexation in the next section.

Comparison of the ^{13}C NMR spectra of **1**H_4 and [Zr(**1**)] is easier, as both compounds show sharp resonances (Figure S68). Most of the signals of the carbon atoms undergo significant upfield shifts, accompanied with scattering. This is the case for 3-C (PIPO component) and 39-C (DFO component), and, to a lesser extent, for 4-C, the atoms of the triads {10-C, 21-C, 32-C}, {11-C, 22-C, 33-C}, and {12-C, 23-C, 34-C}, and of the diad {17-C, 28-C}. Those of the {14-C, 25-C, 36-C} triad and of the {18-C, 29-C} diad move in the opposite direction. In contrast, the following carbon atoms undergo only minor shifts: 5-C, 6-C, and 7-C of the PIPO component, and those of the triad {13-C, 24-C, 35-C}. It is interesting to note that among the methylene carbon atoms linked to the hydroxamate nitrogen atoms, only those of the DFO component (14-C, 25-C, 36-C) show a significant downfield shift ($\Delta\delta = 2.62$–2.73 ppm) upon complexation, as the signal of 6-C does not move. The upfield shifts of the signals of 3-C, 17-C, 28-C, and 39-C are a direct consequence of their proximity with the coordinating hydroxamate carbonyl oxygen atoms. Additional information could be gained from the comparison of the carbonyl regions of the ^{13}C NMR spectra of **1**H_4 and [Zr(**1**)] (Figure S69). In the spectrum of the free ligand, the signals of the carbonyl carbon atoms all resonate between 175 and 173 ppm, the hydroxamic 2-C atom excepted (169.2 ppm). Upon complexation with Zr^{4+}, the signals of the amide carbonyl carbon atoms are slightly moved upfield, between 174.5 and 173.5 ppm, while the signals of the hydroxamate carbonyl carbon atoms are more significantly shifted upfield, including the one of 2-C, between 166.0 and 164.0 ppm.

Through-space dipolar interactions being identified for a certain number of proton pairs of the main diastereomer of [Zr(**1**)], it was tempting to undertake theoretical calculations of the structure of [Zr(**1**)] in order to obtain inter-proton distances and compare, at least qualitatively, the results obtained with the experimental data. Such an endeavor could allow us to unravel characteristic features of the structure of the complex, such as the coordination geometry of the Zr^{4+} cation in the hydroxamate oxygen-atom coordination sphere, the winding of the chelator around the metal, ligand conformational details, and possible stabilizing intramolecular secondary interactions, such as hydrogen bonding.

Structural Studies of [Zr(1)] by DFT Calculations

Determination of the possible theoretical structures of the major diastereomer of [Zr(**1**)] have been performed using the following methodology, which combined molecular dynamics (Amber 12[23]) and quantum chemistry calculations (Gaussian09[24]). Firstly, the stereoelectronic characteristics of **1**$^{4-}$ were determined (conformation optimized by DFT using the B3LYP functional at the 6-31G* level of theory; determination of the atomic charges using ab initio HF/6-31G* calculations). Next, the General Amber Force Field (GAFF) NONBOND parameters of Zr^{4+} were obtained in such a way to reproduce the Zr···O DFT optimized bond distances. Initial conformations of [Zr(**1**)] were then constructed by placing Zr^{4+} by 10 degree increments from $\phi = 0$ to 360° around circles that occupied 17 equally distributed positions on a cylinder of 30 Å diameter threaded along its axis by **1**$^{4-}$ in its fully extended conformation (Figure S71). Molecular dynamics at 300 K starting from these $17 \times 37 = 629$ initial arrangements were followed by simulated annealing at 300 and then 1200 K, while restraining the Zr–O distances between 2.0 and 2.5 Å. The obtained structures were then frozen at 0 K and subsequently optimized at the

B3LYP–D3 DFT level of theory using the 6-31G(d,p) basis set (LANL2DZ ECP for Zr[25]) without any restraint. The final structures were identified using the notation [ϕ.*l*] and [ϕ.*l*N], *l* taking all the even values between −16 and +16, including 0. The RMSD (root mean square deviation) matrix was calculated in order to compare the structures and eliminate the redundant ones. In the end, 1219 structures were obtained, the energy of which ranged from 0 (for [220.2]) to 601.3 kJ mol^{-1} (for [270.2]). Energetic and structural details of the 44 most stable structures are listed in Table S3 together with their Boltzmann probability p_i. The plots of the Boltzmann populations and the corresponding weighted populations are given in Figure S72.

We examined in detail these 44 lowest energy structures out of the 1219 returned by the calculations. They were ranked according to their energy with reference to [220.2], from 0 to 21.5 kJ mol^{-1} (Table S3). The geometries of the Zr^{4+} coordination spheres are schematically drawn in Figure S73, which shows that they encompass 17 different arrangements of the four hydroxamate subunits around Zr^{4+} (labeled A to Q).

27 proton pairs {H1, H2} showing non-trivial rOe correlations, hence constituted of atoms that are bound neither to the same carbon atom, nor to consecutive carbon atoms were identified. Their relative intensities ranged from 0.33 to 1.00. For each of these 44 structures, we measured the bond distances between the protons of a given pair. The proton pairs {H1, H2}, the relative intensities of the rOe, and the shortest H1···H2 distances (*d*) are collected in Table S4, an extract of it being shown in Table 1 for the structures discussed. From the latter, we can see that most of the H1···H2 distances are shorter than 3.1 Å. However, there are two proton pairs showing nearly systematically minimal distances exceeding 4.0 Å, that is, {5a-H, 7-H} and {10b-H, 13a-H}. The proton pairs {28-H, 31-H} show minimal distances around 4 Å, but this occurrence is less systematic. Structures [100.–6 N] (5.0 kJ mol^{-1}) and [90.–16] (9.0 kJ mol^{-1}) are those of lowest energy, for which the calculated distances 5a-H···7-H and 10b-H···13a-H respectively, are <3 Å. The lowest energy structures for which the distances

Table 1. Relative intensities of the rOe correlations between proton pairs {H1, H2} and the minimal distances measured in the lowest energy calculated structures of A-type (5) and B-type (4). The relative energies and the Boltzmann distribution of the structures are indicated, as well as the coordination geometry of Zr^{4+}.

H1	H2	rOe intensity	[220.2]	[140.0]	[340.10]	[100.–6N]	[90.–16]	[0.6N]	[180.–8]	[180.6]	[270.–14]
ΔG (kJ mol^{-1})			0	0.2	5.0	5.0	9.0	10.6	12.0	13.4	16.0
Boltzmann distribution (%)			42.0	38.3	5.6	5.5	1.1	0.6	0.3	0.2	0.1
Structure type			A	A	A	B	A	B	B	A	B
Coordination geometry			BTP	TDD	TDD	TDD	BTP	TDD	BTP	TDD	TDD
4a	6b	0.50	2.702	2.702	2.440	2.663	2.718	2.676	2.726	2.729	2.647
4b	6a	0.67									
5a	7	0.67	4.545[a]	4.540	4.557	2.316	4.551	2.270	4.531	4.528	2.298
4a	7	0.67	2.426	2.436	2.412	2.499	2.412	2.528	2.435	2.443	2.499
7	9[b]	1.00	2.592	2.673	2.420	3.099	2.424	4.041	2.532	2.625	3.384
9	12ab	1.00	2.498	2.459	2.315	2.360	2.137	2.217	2.351	2.419	2.293
10a	12ab	0.50	2.624	2.629	2.641	2.603	3.124	2.818	2.615	2.498	3.430
10b	13a	0.50	4.581	4.578	4.553	4.534	2.220	4.631	4.562	4.137	2.285
12ab	14ab	0.50 (2)[c]	3.071	3.065	2.490	3.106	2.529	2.674	2.450	2.667	2.615
14a	17a	1.00	2.080	2.080	2.094	2.135	2.058	2.218	1.967	1.990	2.042
14a	17b	0.50									
18a	20	1.00	2.224	2.170	2.172	2.231	2.231	2.213	2.282	2.285	2.186
18b	20	0.67									
20	23ab	0.83	3.048	3.048	3.096	3.107	3.054	3.167	2.573	3.173	2.201
21b	23ab	0.33	2.633	2.608	2.609	2.598	2.646	2.625	2.640	2.642	3.262
25ab	28ab	0.50 (2)	2.327	2.384	2.402	2.193	2.353	2.363	2.088	2.138	2.432
28ab	31	0.67	4.163	4.100	4.128	3.836	3.482	4.121	2.409	2.451	4.201
29ab	31	0.67	2.336	2.312	2.312	2.374	2.345	2.244	3.303	3.335	2.217
31	33ab	0.83	2.422	3.105	3.092	2.392	2.429	3.257	2.577	2.299	2.955
31	34a	0.50	2.554	3.202	3.069	2.440	2.566	2.173	2.375	2.916	2.842
34ab	36a	0.33 (2)	2.983	2.837	2.879	2.456	3.000	2.281	2.706	3.179	2.755
36a	39	1.00	2.115	2.338	2.142	2.396	2.132	2.299	2.442	2.095	2.417
36b	39	0.83									

[a] Color code: $d > 4.0$ Å; $3.5 \leq d < 4.0$ Å; $3.1 \leq d < 3.5$ Å; $3.0 \leq d < 3.1$ Å; $d < 3.0$ Å. [b] Protons labels in blue correspond to N*H*. [c] Two correlation spots are observed.

28-H···31-H fall below 3 Å are [240.8], [180.–8], and [180.6], with energies ranging between 11.2 and 13.4 kJ mol^{-1}.

The broad features observed in the ^{1}H NMR spectrum of [Zr(**1**)] could be the result of conformational equilibria occurring at the 500 MHz timescale, and affecting the chains of the atoms connecting consecutive chelate subunits. On the contrary, rearrangements of the chelate subunits in the coordination sphere of Zr^{4+} are too slow to contribute to the broadening of the ^{1}H NMR signals. Therefore, the two species in *ca.* 77 : 23 ratio giving rise to exchange correlation spots in the ROESY map most probably correspond to coordination isomers that give slow exchange signals in the 1D ^{1}H NMR spectrum, that is two among the structures shown in Figure S73. The low number of detectable and identifiable signals of the minor species precludes its structural characterization by comparison of the NMR and calculated data.

In order to select the structure(s) of the major stereoisomer that best account for the NMR observations, it is necessary to have a closer look at the calculated coordination sphere of the zirconium tetracation, which, in the [Zr(**1**)] complex, is eight-coordinated. Most metal complexes in which the metal cation is surrounded by eight monodentate ligands exhibit one of the three following coordination geometries: the square antiprism (SAP), the bicapped trigonal prism (BTP), and the trigonal dodecahedron (TDD), which all contain eight vertices.[26] For example, the X-ray crystal structure analysis of [Zr(PIPO)$_4$] showed that the Zr^{4+} ion displays the SAP coordination geometry.[16] Perspective canonical views of these polyhedra are shown in Figure 4, together with vertex and edge labelling. They can be interconverted into each other by geometrical changes (relative positions of the vertices and lengths of the edges) together with topological changes (addition/deletion of edges, one in the case of the SAP/BTP interconversion, two in the case of the SAP/TDD interconversion). The dotted colored edges in the BTP and the TDD are the edges that must be added to the SAP in order to obtain these polyhedra, respectively. Figure 4d shows the view along the C_4 symmetry axis of the SAP, and Figures 4b and 4f show the corresponding views of the polyhedra having the topology of the BTP and the TDD, but displaying the "ideal" SAP geometry.

Let us take the structure of lowest energy [220.2] as an example. A stick view of [220.2] down the pseudo-C_4 symmetry axis of [Zr(**1**)] in an idealized SAP geometry is shown in Figure 5a. The $PIPO^-$-derived chelate subunit (1-O, 2-O) is placed along the front-right edge of the upper square and is followed by the C(O)NHC$_5$(1) spacer, which spans the vertical edge in the anticlockwise direction; the second hydroxamate chelate (15-O,16-O) is placed along the edge in the back of the lower square and followed by the C$_2$(1)C(O)NHC$_5$(2) sequence, which spans the vertical edge in the clockwise direction; the third hydroxamate chelate (26-O, 27-O) is located along the upper-left edge of the upper square and followed by the C$_2$(2)C(O)NHC$_5$(3) sequence, which spans the vertical edge in the anticlockwise direction; finally, the fourth hydroxamate chelate (37-O, 38-O) occupies the edge in the front of the lower square, so that 38-O is connected to 1-O and 2-O by vertical edges. We give the label "A" to this arrangement of the chelator around Zr^{4+}. Schematical drawings are shown in Figures 6a and 6b. In these drawings, the emboldened edges colored in blue represent the chelates and those in red represent the bridges between the chelates. The vertices are marked with numbered red disks that stand for the oxygen atoms of the hydroxamate groups.

Actually, the coordination geometry of Zr^{4+} in the theoretical structure [220.2] is closer to BTP than TDD and SAP according to Continuous Shape Measure (CShM) analysis,[27] as the CShM values are 1.49, 1.57, and 1.92, respectively (Table S3). The next structures, [140.0] (0.2 kJ mol^{-1}) and [340.10] (5.0 kJ mol^{-1}) are much closer to TDD than BTP and SAP (see Table S3 and Figure S74), but views along the pseudo-C_4 symmetry axis show that they display the same chelate arrangement (type A) around Zr^{4+} and differ from structure [220.2] by the conformation of the C$_5$(3) spacer for [140.0], and both C$_5$(1) and C$_5$(3) spacers for [340.10]. The coexistence of these three structures, which account for nearly 86% of the Boltzmann distribution, could indeed explain the broad features observed in the 3.8–2.9 and 1.8–1.2 ppm regions of the ^{1}H NMR spectrum,

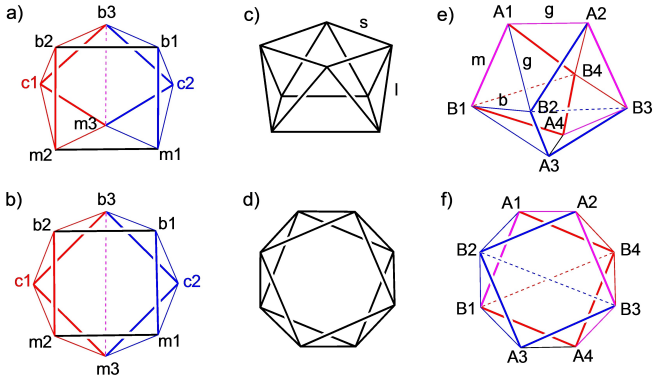

Figure 4. The three most frequently encountered coordination geometries of ML$_8$-type complexes: a) bicapped trigonal prism (BTP); c) side view and d) top view of the square antiprism (SAP); e) trigonal dodecahedron (TDD). BTP is obtained from SAP by addition of the b3m3 edge and moving m3 in such a way that the triangles b1b2b3 and m1m2m3 are parallel to each other. DD is obtained from SAP by addition of the B2B3 and B1B4 edges. The views b) and f) show how SAP and TDD derive from BTP. The sequences of edges corresponding to the squares of the SAP are embolded in the views of BTP and TDD.

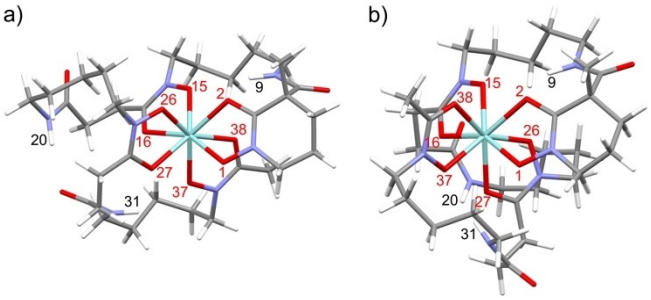

Figure 5. Stick representations viewed down the pseudo-C_4 symmetry axis of the calculated structures (a) [220.2], and (b) [100.–6N] of [Zr(**1**)] in an idealized SAP geometry. Numbers in red show the labels of the hydroxamate oxygen atoms; numbers in black show the labels of the amide protons (white rods in the stick representation).

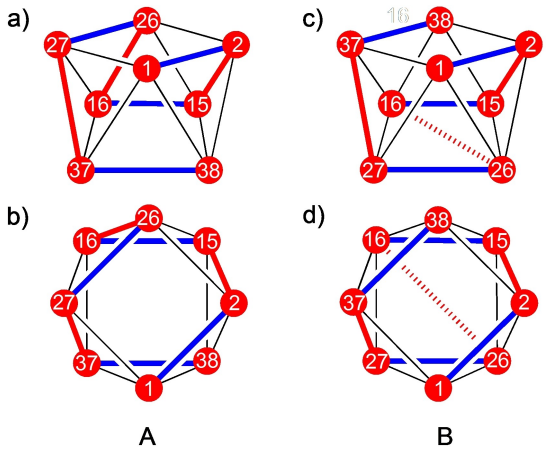

Figure 6. Schematic drawings, in the ideal SAP coordination geometry, of the winding modes A and B of the chelator $\mathbf{1}^{4-}$ in the calculated structures of the [Zr(**1**)] complex [220.2] (a and b) and [100.–6N] (c and d), respectively. In these drawings, the emboldened edges colored in blue are spanned by the hydroxamates, those in red represent the bridges between the binding units. The vertices are marked with numbered red disks that stand for the oxygen atoms of the hydroxamate chelates (positions 1, 15, 26, and 37 correspond to O_N atoms, while 2, 16, 27, and 38 to O_C ones).

as the signals of the protons belonging to the $C_5(1)$ and $C_5(3)$ spacers are located in these regions. The next structure displaying the winding mode A is [90.–16] at an energy of 9.0 kJ mol^{-1}. The coordination geometry of Zr^{4+} in [90.–16] is closer to the BTP than in [220.2] (CShM = 1.34 *vs.* 1.49, see Table S3). The view of structure [90.–16] along its pseudo-C_4 symmetry axis is also shown in Figure S74. It differs from [220.2] by the conformation of the $C_5(1)$ spacer. Noticeably, all of the four structures studied so far show more-or-less the same conformations of the $C_5(2)$ chains, as well as the $C_2(1)$ and $C_2(2)$ bridges between the hydroxamic and amide carbonyl functions. The next lowest energy structure of type A is [180.6] at 13.4 kJ mol^{-1}. Remarkably, it shows the shortest 28-H···31-H distance of 2.451 Å.

We now turn to structures of type B, for which the arrangement of the chelator is drawn schematically in Figures 6c and 6d. The lowest energy B-type structure is [100.–6N]. Its energy is 5 kJ mol^{-1} above that of [220.2]. The view down the pseudo-C_4 symmetry axis (Figure 5b) indicates that the arrangement of two of the three DFO hydroxamate subunits of $\mathbf{1}^{4-}$ differs from that found in the structures of type A. Whereas the first two binding units of $\mathbf{1}^{4-}$, (1-O, 2-O) and (15-O, 16-O), are placed as in [220.2] and the related structures, the third hydroxamate group (26-O, 27-O) is located along the front edge of the lower square from the right to the left, the connection between 16-O and 26-O spanning the corresponding diagonal of the lower square. The fourth chelating unit (37-O, 38-O) is located on the back left edge of the upper square, being parallel to the first chelate (1-O, 2-O). The next lowest energy structure of type B is [0.6 N] (10.6 kJ mol^{-1}), which differs from [100.–6N] by the conformations of the $C(O)NHC_5(1)$ and $C_2(2)C(O)NHC_5(3)$ spacers (Figure S75). Again, the conformations of the $C_2(1)C(O)NHC_5(2)$ spacers in these two structures do not differ significantly, as in the case of the structures [220.2], [140.0], [340.10], and [90.–16]. The geometry of the coordination sphere of Zr^{4+} in [100.–6N] and [0.6N] is very close to TDD (CShM values of 0.83 and 0.84, respectively, see Table S3 and Figure S75). The next lower energy structures having the configuration B are [180.–8] (12.0 kJ mol^{-1}) and [270.–14] (16.0 kJ mol^{-1}). [180.–8] differs from [100.–6N] by the conformations of the $C_5(1)$, $C_5(2)$, and the $C_2(2)C(O)NHC_5(3)$ spacers, and [270.–14], by the conformations of the $C_5(1)$, $C_5(2)$, and the $C_2(2)C(O)NHC_5(3)$ spacers. Among the 44 lowest energy structures, those labeled A and B represent the highest occurrences, respectively 27 and 18 %, between the two of them they have a total of 45 %.

We now examine the interproton distances for which non-trivial rOe correlations have been identified in the nine lowest energy structures shown in Table 1. A color code has been used to highlight the following distance ranges: $4.0 < d < 5.0$ Å in red, $3.5 \leq d < 4.0$ Å in violet, $3.1 \leq d < 3.5$ Å in blue, $3.0 \leq d < 3.1$ Å in green, and $d < 3.0$ Å in black. This code allows the reader to notice that most of the distances are < 3.0 Å. We make an inventory of the distances $4.0 < d < 5.0$ Å, as this range includes the upper distance limit to account for the relatively intense (0.50–0.67) corresponding rOe cross-peaks.[28] All the nine structures listed in Table 1 include at least one and at most three distances $4.0 < d < 5.0$ Å, which involve the proton pairs {5a-H, 7-H}, {10b-H, 13a-H}, and {28ab-H, 31-H} in most cases, and {7-H, 9-H} in one case. The three lowest energy structures (A-type) [220.2], [140.0], and [340.10] show two distances slightly above 4.5 Å, and one distance slightly above 4.1 Å. By contrast, the next A-type structures, [90.–16] and [180.6], show only one and two distances over 4.0 Å, respectively. The lowest energy B-type structure, [100.–6N], shows only one distance greater than 4.0 Å, while the two next B-type structures, [0.6N] and [180.–8], show three and two distances greater than 4.0 Å, respectively. The highest energy B-type structure has only one distance over 4.0 Å. Therefore, overall, a maximum of 3 over 26 interproton distances exceed 4.0 Å, but remain lower than 5.0 Å in the nine structures detailed. In addition to this observation, it is important to note that the non trivial rOe's listed in Table 1 are all consistent with the nine lowest energy structures of type A and B, and that it was not possible to find any rOe, which could be accounted for by only one particular structure.

In summary, the three lowest energy structures show three interproton distances higher than 4 Å, whereas two of the type B structures show only one. Actually, the differences, in terms of interproton distances, are not that decisive. Therefore, we shall fall in with the arbitrament of theory: The four lowest energy structures of the A-type arrangement represent 87 % of the calculated Boltzmann population, therefore they should be considered as more probable than those of the B-type arrangement, which represent only 6.5 % of this population.

We therefore assume that the broad features of the 500 MHz ^{1}H NMR spectrum of [Zr(**1**)] are accounted for by a set of exchanging conformations of the chelator displaying the A-type arrangement. Table S5 summarizes selected structural features of the four lowest energy conformations of type A and type B arrangements, respectively, that is, the metrics of the

Zr^{4+} coordination sphere and the lengths of the intramolecular hydrogen bonds between the amide protons and either bound hydroxamate or amide oxygen atoms. The minimal and maximal Zr–O bond distances are 2.152 and 2.296 Å, respectively, the average value being 2.220 Å. The O–Zr–O bite angles range between 68.58 and 70.20°, the average value being 69.30°. These parameters are in very good agreement with the experimental values measured for the crystal structure of [Zr(PIPO)$_4$] (Zr–O = 2.20(2) and O–Zr–O = 70.2(4)°).[16] Referring to a statistical study of hydrogen bonds in amino acids and peptides (H···O distances ≤ 2.4 Å, N–H···O angles between 120 and 180°),[29] a few true intramolecular hydrogen bonds could be detected in the structures between the amide protons 9-H, 20-H, or 31-H and either bound hydroxamate (2-O_C, 27-O_C, 26-O_N, or 37-O_N) or amide (30-O) carbonyl oxygen atoms (Table S5). All three amide protons are engaged in an intramolecular hydrogen bond, 9-H with the hydroxamate carbonyl 2-O atom for all eight structures, [0.6N] excepted, and the hydroxamate 26-O_N for [0.6N], 20-H with the carbonyl 30-O atom for all eight structures, [100.–6N] and [270.–14] excepted, and 31-H with the hydroxamate carbonyl 27-O atom for all eight structures, [220.2], [90.–16], and [270.–14] excepted, and with the hydroxamate 37-O_N for [140.0], [340.10], and [100.–6N]. The sign and magnitudes of the complexation induced shifts of the amide protons 9-H (+0.388 ppm), 20-H (+0.112 ppm), and 31-H (+0.255 ppm) (Table S2), further confirm that they are engaged in intramolecular hydrogen bonds in the complex and that the most affected is 9-H. This latter fact could be a consequence of the number (7/8) of conformations exhibiting the 9-H···2-O hydrogen bond is the highest.

Figure 7 shows views of the coordination polyhedra of Zr^{4+} in the two lowest energy structures, [220.2] (0 kJ mol^{-1}) and [140.0] (0.2 kJ mol^{-1}), which have the A-type arrangement, the BTP and the TDD coordination geometries, respectively, and the two low energy structures of the B-type arrangement that have the TDD and the BTP coordination geometries, respectively: [100.–6N] (5.0 kJ mol^{-1}) and [180.–8] (12 kJ mol^{-1}). These polyhedra are displayed in the same fashion as in the ideal SAP of Figure 4c. The calculated dihedral angles δ between triangular faces sharing an edge are collected in Table S6 for all four structures. The quadrilaterals showing the less marked folds are easy to identify: They have the vertices 15-O, 16-O, 37-O, and 38-O in the case of [220.2], and 1-O, 2-O, 37-O, and 38-O in the case of [180.–8]. Therefore, referring to Figure 4a we can make the following 1:1 correspondences between the vertices 1-O, 2-O, 15-O, 16-O, 26-O, 27-O, 37-O, and 38-O and those of the BTP: For [220. 2], with m3, c1, b2, b1, b3, c2, m1, and m2, and for [180.–8], with b1, b2, c1, m3, b3, c2, m1, and m2. As shown in Table S6, the highest changes of dihedral angles upon going from [220.2] to [140.0], on the one hand, and [100.–6N] to [180.–8], on the other hand, concern those along the (16-O, 38-O) edge for [220.2], and the (1-O, 38-O) edge for [180.–8]. The small values of the $\Delta\delta$ suggest that the interconversion between the TBP and the TDD should occur at almost the same time scale as the ^{1}H NMR measurements according to the observed line broadening. A contrario, the interconversion between A-type structures and B-type structures should not be feasible at the NMR timescale. As two diastereomers are observed in a ratio (77:23) that is not that far from the ratio between the Boltzmann populations of the A-type and B-type structures (93:7), it could be possible that the major diastereomer corresponds indeed to A-type arrangements, while the minor diastereomer would correspond to B-type ones.

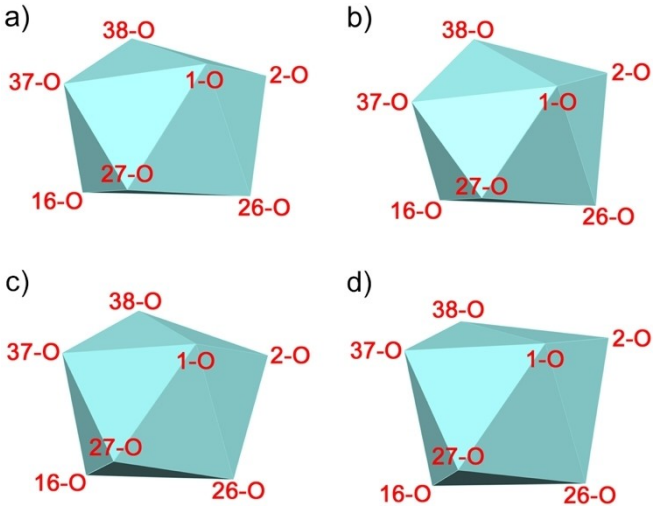

Figure 7. Coordination polyhedra of Zr^{4+} in the calculated structures (a) [220.2], (b) [140.0], (c) [100.–6N], and (d) [180.–8] of [Zr(**1**)$_4$]. The visible vertices (7 out of 8) are identified by the labels of the pairs of hydroxamate oxygen atoms corresponding to the four chelate subunits {1-O, 2-O}, {15-O, 16-O}, {26-O, 27-O}, and {37-O, 38-O}, 15-O being hidden in the back.

Conclusions

In this work we have reported the synthesis of the chelator **1**H$_4$, which derives from (DFO)H$_3$ by appending a natural cyclic hydroxamic acid chelating subunit derived from 1-hydroxy-2-piperidone, (PIPO)H. **1**H$_4$ is chiral because the 6-membered (PIPO)H ring component contains an asymmetric carbon atom, but **1**H$_4$ was obtained herein as a racemate.

The complex [Zr(**1**)] was prepared, characterized, and its solution structure investigated by a battery of NMR experiments. In methanol, [Zr(**1**)] exists as a mixture of two diastereomers in *ca.* 77:23 ratio that do not exchange at the ^{1}H and ^{13}C NMR timescales. We focused our study on the major diastereomer, the ^{1}H NMR spectrum of which exhibits broad features, while its ^{13}C NMR spectrum is well resolved. We could assign their signals to all the protons, the nitrogen, and the carbon atoms of the complex using a combination of ^{1}H/^{1}H ROESY and pure-shift TOCSY, pure-shift ^{13}C/^{1}H HSQC, ^{13}C/^{1}H H2BC, ^{13}C/^{1}H HMBC, and ^{15}N/^{1}H HMBC experiments. Several through-space rOe correlations involving protons pairs separated by more than three bonds, indicated that these protons were close in space, in spite of their topological distance, as the result of the winding of the chelator around the metal cation. Therefore, we undertook structure calculations using the density-functional theory (DFT) for optimizing the geometry of 629 starting arrangements. More than 1000 structures were returned by the calculations. The 44 of lowest energy, which

accounted for more than 99.4% of the calculated Boltzmann population, were analyzed in detail in terms of the Zr^{4+} coordination sphere, the winding of the chelator around the metal cation, and inter-proton distances. Two types of structures (A and B), differing by the arrangement of the chelator, came out of the 17 different structural types (A–Q) identified within the set of 44 investigated, their occurrence representing 45% of the latter.

The solution structural NMR study reported herein indicates that $\mathbf{1}^{4-}$ could still be optimized for Zr^{4+} chelation, as the chirality at the 3-C carbon atom of the tetraanion is not fully transferred to the metal cation, the complex existing in solution in the form of two diastereomers. As the ligand incorporates DFO^{3-}, which brings three of the four hydroxamate binding subunits, we can improve its capacity to complex Zr^{4+} stereoselectively by playing only with the nature of the fourth chelating group and the nature of the spacer that connects it to the DFO fragment. Work along these lines is in progress and will be reported in due course.

Experimental Section

Materials. The abbreviations used are the following: HMDS (hexamethyldisilazane), THF (tetrahydrofuran), DMF (*N*,*N*-dimethylformamide), EDC·HCl (1-ethyl-3-(3-dimethylaminopropyl)carbodiimide hydrochloride), HOBt (1-hydroxybenzotriazole), DIPEA (diisopropylethylamine). Unless otherwise stated, the reactions were carried out under an argon atmosphere, using Schlenk techniques. All solvents and analytical-grade chemicals were obtained from commercial suppliers and used without further purification. Desferriferrioxamine B was purchased as its mesylate salt ([(DFO)H_4](CH_3SO_3), Desferal®) from Apollo Scientific Ltd and used as received after checking its purity by HPLC. Pentanoic acid, 5-[(ethoxycarbonyl)(phenylmethoxy)amino]ethylester (**2**) and ethyl 1-(benzyloxy)-2-oxopiperidine-3-carboxylate (**3**) were synthesized according to the literature.[21] Diisopropylethylamine was dried by distillation from potassium hydroxyde pellets under argon. The solvents were dried as follows: THF by reflux over sodium/benzophenone ketyl or by flowing through an alumina column, acetone by reflux over potassium carbonate, followed by distillation under argon. DMF was dried by stirring with magnesium sulfate, then distilled in vacuum at 40 °C and stored under argon on 3 Å molecular sieves. HPLC grade methanol and analytical grade acetone were used as received. Manual chromatographic separations were performed by flash column chromatography using 40–60 μm silicagel 60.

Instrumentation. Chromatographic separations were also performed using an Interchim™ Puriflash 4125 system equipped with an injector (10 mL loop or solid-state deposit using Celite as inert matrix), a fraction collector, UV (260 nm) and ELSD detectors. Normal phase separations were performed using prepacked columns (spherical particle size: 30 μm diameter, 4 to 120 g) and reverse phase purifications were done using C18-AQ Interchim™ prepacked columns (particle size: 15 μm, 24 g) at a flow rate of 15 mL min^{-1} for columns of 25 g capacity and 26 mL min^{-1} for larger ones.

Physical measurements were performed either at the technological platform for chemical analysis and molecular synthesis of the Institut de Chimie Moléculaire de l'Université de Bourgogne in Dijon (PACSMUB, http://www.wpcm.fr) or at the Fédération de Chimie "Le Bel" in Strasbourg. ^{1}H and $^{13}C\{^1H\}$ NMR spectra were recorded on Bruker spectrometers operating either at 500 MHz (Bruker Avance III), or 600 MHz (Bruker Avance II) using $CDCl_3$ or CD_3OD as solvents. Chemical shifts on the δ scale (ppm) relative to tetramethylsilane were referenced internally with respect to either the protio resonance of residual $CHCl_3$ ($\delta_H = 7.26$ ppm and $\delta_C = 77.16$ ppm) or CH_3OH ($\delta_H = 3.31$ ppm and $\delta_C = 49.00$ ppm). The ROESY experiment was performed at 500.13 MHz with a mixing time of 200 ms. Fourier-transform mid-infrared (400–4000 cm^{-1}) spectra (FTIR) were recorded at 4 cm^{-1} resolution on a Bruker VERTEX 70v spectrometer fitted with an A225 diamond ATR accessory (Bruker) and a DTGS detector (350–4000 cm^{-1}). High-resolution electrospray ionization mass spectra (HR ESI MS) were recorded on an LTQ XL Orbitrap (Thermo Scientific) machine equipped with an electrospray ionization source (HESI) and the data processed with the Thermo Xcalibur 3.0.63 software. Calibration in the 200–2000 Da mass range was performed using the Pierce LTQ ESI Positive ion Calibration solution (88322-TK275676). Spectra were acquired in the positive mode in the *m*/*z* range 200–2000 using following settings: HESI heater temperature = 50 °C; ionization spray voltage = 4 kV; capillary temperature = 275 °C; capillary voltage = 22 V; tube lens = 110 V; sheath, auxiliary, and sweep gas flows were set to 15, 10, and 0; resolution = 60000 at *m*/*z* = 400.

Compound 7. [(DFO)H_4](CH_3SO_3) (1.495 g, 2.28 mmol), carboxylic acid **5** (0.600 g, 2.28 mmol), EDC·HCl (0.657 g, 3.42 mmol), and HOBt (0.523 g, 3.42 mmol) were introduced in a Schlenk flask under an argon atmosphere. DIPEA (1.935 mL, 11.4 mmol) diluted in DMF (45 mL) was then introduced and the reaction mixture was stirred for 4 d at 40 °C. The solvent was evaporated to dryness and the residue was acidified with an aqueous solution of acetic acid (20 mL, 0.85 M). The solution was concentrated *in vacuo* and the crude compound purified by reverse phase flash chromatography (C18-AQ) using H_2O/MeCN as eluent (95:5 to 0:100 gradient). The desired product was obtained as a pale beige-orange powder (1.450 g, 79%). Mp 106.1–107.3 °C. ^{1}H NMR (600.23 MHz, CD_3OD, 300 K): $\delta = 7.905$ (br q, 1 H; 31-H), 7.600 (br t, 2 H; 9-H and 20-H), 7.459 (m, 2 H; o-H), 7.396–7.351 (m, 3 H; m-H and p-H), 4.950 (AB, $^2J_{AB} = 10.5$ Hz, $\Delta\nu = 11.6$ Hz, 2 H; PhCH_2), 3.606–3.577 (m, 6 H; 14-H, 25-H, and 36-H), 3.472 (m, 2 H; 6-H), 3.209 (m, 2 H; 10-H), 3.184–3.144 (m, 4 H; 21-H and 32-H), 2.762 (t, $^3J_{H,H} = 7.2$ Hz, 4 H; 17-H and 28-H), 2.450 (t, $^3J_{H,H} = 7.2$ Hz, 4 H; 18-H and 29-H), 2.295 (ddd, $^2J_{H,H} = 13.8$ Hz, $^3J_{H,H} = 6.3$ Hz, $^3J_{H,H} = 3.6$ Hz, 1 H; 4a-H), 2.091 (s, 3 H; 39-H), 1.798 (m, 2 H; 5-H), 1.668–1.604 (m, 6 H; 13-H, 24-H, and 35-H), 1.569 (ddd, $^2J_{H,H} = 13.8$ Hz, $^3J_{H,H} = 10.2$ Hz, $^3J_{H,H} = 4.2$ Hz, 1 H; 4b-H), 1.557–1.490 (m, 6 H; 11-H, 22-H, and 33-H), 1.428 (s, 3 H; 7-H), 1.360–1.311 (m, 6 H; 12-H, 23-H, and 34-H) ppm. ^{13}C NMR (150.93 MHz, CD_3OD, 300 K): $\delta = 174.9$ (19-C and 30-C), 174.5 (16-C and 27-C), 174.2 (8-C), 173.5 (38-C), 170.9 (2-C), 136.5 (i-C), 130.9 (o-C), 129.9 (p-C), 129.5 (m-C), 76.4 (PhCH_2), 52.8 (3-C), 51.6 (6-C), 48.9 (hidden; 14-C, 25-C, and 36-C), 40.6 (10-C), 40.3 (21-C and 32-C), 32.7 (4-C), 31.5 (2 s; 18-C and 29-C), 30.0 (3 s; 11-C, 22-C, and 33-C), 29.0 (2 s; 17-C and 28-C), 27.3 (br s; 13-C, 24-C, and 35-C), 24.9 (2 s; 12-C, 23-C, and 34-C), 24.6 (7-C), 21.2 (5-C), 20.2 (39-C) ppm. IR (ATR): $\nu = 3309$ (w), 3108 (br, w), 2928 (w), 2825 (w), 1617 (vs), 1558, 1455, 1424, 1396, 1376 (m), 1311 (vw), 1254, 1224, 1194, 1159 (w), 1086, 1044, 1018, 993, 960, 921, 879, 764 (w), 727 (m) cm^{-1}. Elemental analysis: Calcd (%) for $C_{39}H_{63}N_7O_{11}\cdot 0.6H_2O$ (816.78 g/mol): C 57.35, H 7.92, N 12.00; found: C 57.22, H 8.02, N 12.53. HR-MS (ESI): Calcd for $C_{39}H_{63}N_7O_{11} + Na^+$, 828.44778; found 828.44700.

Compound 1H_4. A Pd/C suspension (10% Pd, 50% water; 0.233 g, 0.13 mmol) was added to a solution of compound **7** (0.336 g, 0.42 mmol) in methanol (32 mL). The reaction mixture was degassed and placed under dihydrogen (1 atm). The reaction was stirred for 2 h at room temperature. The catalyst was filtered off

over a Millipore membrane, affording $\mathbf{1}H_4$, after removal of the solvents, as a colorless solid (0.277 g, 95% yield). Mp 116.3–118.3 °C. ^{1}H NMR (600.23 MHz, CD_3OD, 300 K): $\delta = 7.920$ (br s, 2 H; 20-H and 31-H), 7.644 (br t, 1 H; 9-H), 3.623 (m, 2 H; 6-H), 3.613–3.582, average 3.598 (m, 6 H; 14-H, 25-H, and 36-H), 3.201 (m, 1 H; 10-H), 3.167 (t, $^3J_{H,H} = 7.2$ Hz, 4 H; 21-H and 32-H), 2.766 (t, $^3J_{H,H} = 7.2$ Hz, 4H; 17-H and 28-H), 2.455 (2 t, $^3J_{H,H} = 7.2$ Hz, 4 H; 18-H and 29-H), 2.357 (ddd, $^2J_{H,H} = 13.5$ Hz, $^3J_{H,H} = 6.3$ Hz, $^3J_{H,H} = 3.0$ Hz, 1 H; 4a-H), 2.093 (s, 3 H; 39-H), 1.994–1.824, average 1.909 (m, 2 H; 5-H), 1.656–1.610, average 1.633 (m, 6 H; 13-H, 24-H, and 35-H), 1.636 (hidden, 1 H; 4b-H), 1.553–1.499, average 1.526 (m, 6 H; 11-H, 22-H, and 33-H), 1.434 (s, 3 H; 7-H), 1.363–1.308, average 1.336 (m, 6 H; 12-H, 23-H, and 34-H) ppm. ^{13}C NMR (150.93 MHz, CD_3OD, 300 K): $\delta = 174.9$ (19-C and 30-C), 174.5 (16-C and 27-C), 174.4 (8-C), 173.5 (38-C), 169.2 (2-C), 52.4 (6-C), 51.9 (3-C), 48.7 (hidden; 14-C, 25-C, and 36-C), 40.6 (10-C), 40.3 (21-C and 32-C), 32.8 (4-C), 31.5 (2 s; 18-C and 29-C), 30.0 (2 s; 11-C, 22-C, and 33-C), 29.0 (2 s; 17-C and 28-C), 27.3 (13-C, 24-C, and 35-C), 24.9 (2 s; 12-C, 23-C, and 34-C), 24.8 (7-C), 21.1 (5-C), 20.2 (39-C) ppm. ^{15}N/^{1}H HMBC (60.83/600.23 MHz, CD_3OD, 300 K): $\delta = -201.6$ (37-N), −203 (15-N and 26-N), −203.6 (1-N), −260 (20-N and 31-N), −265 (9-N) ppm. IR (ATR): $\nu = 3311$ (s, br), 3188 (m, br), 2930 (m), 1728 (w), 1619 (vs), 1552 (m), 1453 (m), 1312 (vw), 1257, 1196, 1159 (w), 1003, 955, 926, 876, 768 (vw), 727 (w) cm^{-1}. Elemental analysis: Calcd (%) for $C_{32}H_{57}N_7O_{11}$ (715.85 g mol^{-1}): C 53.69, H 8.03, N 13.70; found, C 52.91, H 8.83, N 13.53. HR-MS (ESI): Calcd for $C_{32}H_{57}N_7O_{11} + Na^+$, 738.40083; found 738.39888.

Complex [Zr(1)]. A solution of $[Zr(acac)_4]$ (0.068 g, 0.14 mmol) in methanol (2 mL) was added to a solution of $\mathbf{1}H_4$ (0.100 g, 0.14 mmol) in methanol (2 mL). The reaction mixture was stirred at room temperature overnight. The solvent was evaporated and the residue dried at 40 °C before it was dissolved in methanol (2.4 mL). The solution was clarified by filtration, the solvent was removed again under reduced pressure, and the residue dissolved in methanol at 65 °C (1 mL). The solution was layered with acetone (10 mL). Upon cooling to room temperature, a solid material precipitated. After further addition of acetone (4 mL), the flask was stored at −18 °C. The precipitate was filtered off, washed with acetone, dried in the air, then under vacuum. This procedure afforded [Zr(**1**)] in pure form as a colorless solid (0.0356 g, 32%). ^{1}H NMR (600.23 MHz, CD_3OD, 300 K) for the major stereoisomer: $\delta =$ 8.175 (br t, 1 H; 31-H), 8.032 (br m, 1 H; 9-H and 20-H), 3.954 (1 H; 14a-H), 3.747 (1 H; 36a-H), 3.694 (1 H; 25a-H), 3.682 (1 H; 6a-H), 3.631 (1 H; 6b-H), 3.560 (1 H; 25b-H), 3.537 (1 H; 14b-H), 3.500 (1 H; 36b-H), 3.442 (1 H; 10a-H), 3.415 (1 H; 21a-H), 3.333 (1 H; 32a-H), 3.097 (1 H; 32b-H), 3.086 (1 H; 10b-H), 3.085 (1 H; 21b-H), 2.825 (1 H; 17a-H), 2.743 (2 H; 28a-H and 28b-H), 2.635 (2 H; 18a-H and 29a-H), 2.515 (2 H; 17b-H and 29b-H), 2.404 (1 H; 18b-H), 2.338 (1 H; 4a-H), 2.134 (s, 3 H; 39-H), 2.087 (1 H; 13a-H), 1.942 (1 H; 5a-H), 1.878 (1 H; 5b-H), 1.725 (1 H; 35a-H), 1.685 (2 H; 24a-H and 24b-H), 1.653 (1 H; 11a-H), 1.619 (1 H; 35b-H), 1.592 (1 H; 4b-H), 1.583 (1 H; 22a-H), 1.545 (2 H; 33a-H and 33b-H), 1.519 (1 H; 11b-H), 1.443 (1 H; 13b-H), 1.441 (1 H; 22b-H), 1.398 (s, 3 H; 7-H and 1 H; 34a-H), 1.308 (2 H; 23a-H and 23b-H), 1.304 (2 H; 12a-H and 12b-H), 1.275 (1 H; 34b-H) ppm. ^{13}C NMR (150.93 MHz, CD_3OD, 300 K): $\delta = 174.4$ (19-C or 30-C), 174.2 (19-C or 30-C), 173.7 (8-C), 165.7 (16-C or 27-C), 165.1 (16-C or 27-C), 164.8 (2-C), 164.1 (38-C), 52.3 (6-C), 51.4 (2 s; 14-C, 25-C, or 36-C), 51.3 (14-C, 25-C, or 36-C), 48.8 (hidden; 3-C), 39.7 (32-C), 39.5 (21-C), 38.8 (10-C), 32.5 (29-C), 32.0 (18-C), 31.6 (4-C), 29.1 (22-C), 28.6 (33-C), 27.9 (11-C), 27.7 (35-C), 27.5 (24-C), 27.1 (28-C), 26.6 (13-C), 26.4 (17-C), 24.9 (7-C), 23.4 (12-C and 34-C), 22.7 (23-C), 20.9 (5-C), 17.2 (39-C) ppm. ^{15}N/^{1}H HMBC (60.83/600.23 MHz, CD_3OD, 300 K): $\delta = -172.9$ (37-N), −173.1 (15-N), −173.6 (1-N), −173.8 (26-N), −260.2 (31-N), −260.6 (9-N, 20-N) ppm. Elemental analysis: Calcd (%) for $C_{32}H_{53}N_7O_{11}Zr{\cdot}3H_2O$ (857.08 g mol^{-1}): C 44.84, H 6.94, N 11.44; found, C 44.76, H 7.01, N 11.43. HR-MS (ESI): Calcd for $C_{32}H_{53}N_7O_{11}Zr + H^+$, 802.2923; found 802.2898.

Supporting Information

Experimental section; description of the procedure followed for the assignment of the ^{1}H, ^{13}C, and ^{15}N NMR spectra of [Zr(**1**)]; copies of the ^{1}H, ^{13}C, ^{1}H/^{1}H, and ^{13}C/^{1}H NMR spectra of all the compounds and of the ^{15}N/^{1}H NMR spectrum of [Zr(**1**)]; initial conditions of the DFT calculations; Boltzmann distribution of all the calculated structures; views of the lowest energy structures; tables of the ^{1}H, ^{13}C, and ^{15}N NMR chemical shifts, rOe, and DFT structural data.

Acknowledgements

This work was financially supported by the Centre National de la Recherche Scientifique (CNRS), the Conseil Régional de Bourgogne (CRB, program PARI II CDEA), the European Regional Development Fund (FEDER), the French program "NEEDS Environnement", and the Agence Nationale de la Recherche (ANR project PLUTON, grant N° ANR-17-CE08-0053). F. M. thanks the Université de Bourgogne for funding her post-doctoral fellowship and O. F. the Conseil Régional de Bourgogne and FEDER for his PhD grant (contract n° 2017-9205AAO033S02120). The EXPLOR mesocenter is thanked for providing access to their computing facility (project 2021CPMXX2483). We are grateful to Dr. Laurent Raibaut (Université de Strasbourg) for recording the LC-MS of [Zr(**1**)].

Conflict of Interests

The authors declare no conflict of interest.

Data Availability Statement

The data that support the findings of this study are available in the supplementary material of this article.

Keywords: Ab initio calculations · Chelates · NMR spectroscopy · O ligands · Zirconium

[1] a) M. A. Deri, B. M. Zeglis, L. C. Francesconi, J. S. Lewis, *Nucl. Med. Biol.* **2013**, *40*, 3–14; b) S. Heskamp, R. Raavé, O. Boerman, M. Rijpkema, V. Goncalves, F. Denat, *Bioconjugate Chem.* **2017**, *28*, 2211–2223; c) J. R. Dilworth, S. Pascu, *Chem. Soc. Rev.* **2018**, *47*, 2554–2571; d) N. B. Bhatt, D. N. Pandya, T. J. Wadas, *Molecules* **2018**, *23*, 638; e) L. Melendez-Alafort, G. Ferro-Flores, L. De Nardo, B. Ocampo-García, C. Bolzati, *Coord. Chem. Rev.* **2023**, *479*, 215005.
[2] J. M. Link, K. A. Krohn, J. F. Eary, R. Kishore, T. K. Lewellen, M. W. Johnson, C. C. Badger, K. Y. Richter, W. B. Nelp, *J. Labelled Compd. Radiopharm.* **1986**, *23*, 1297–1298.
[3] I. Verel, G. W. M. Visser, R. Boellaard, M. Stigter-van Walsum, G. B. Snow, G. A. M. S. van Dongen, *J. Nucl. Med.* **2003**, *44*, 1271–1281.

[4] P. K. E. Börjesson, Y. W. S. Jauw, J. C. Roos, J. A. Castelijns, C. R. Leemans, G. A. M. S. van Dongen, R. Boellaard, *J. Nucl. Med.* **2009**, *50*, 1826–1836.
[5] R. Codd, T. Richardson-Sanchez, T. J. Telfer, M. P. Gotsbacher, *ACS Chem. Biol.* **2018**, *13*, 11–25.
[6] G. Schwarzenbach, K. Schwarzenbach, *Helv. Chim. Acta* **1963**, *46*, 1390–1400.
[7] S. Dhungana, P. S. White, A. L. Crumbliss, *J. Biol. Inorg. Chem.* **2001**, *6*, 810–818.
[8] a) W. E. Meijs, J. D. M. Herscheid, H. J. Haisma, H. M. Pinedo, *Appl. Radiat. Isot.* **1992**, *43*, 1443–1447; b) W. E. Meijs, H. J. Haisma, R. P. Klok, F. B. van Gog, E. Kievit, H. M. Pinedo, J. D. M. Herscheid, *J. Nucl. Med.* **1997**, *38*, 112–118.
[9] a) J. P. Holland, V. Divilov, N. H. Bander, P. M. Smith-Jones, S. M. Larson, J. S. Lewis, *J. Nucl. Med.* **2010**, *51*, 1293–1300; b) L. R. Perk, M. J. W. D. Vosjan, G. W. M. Visser, M. Budde, P. Jurek, G. E. Kiefer, G. A. M. S. van Dongen, *Eur. J. Nucl. Med. Mol. Imaging* **2010**, *37*, 250–259; c) N. Pandit-Taskar, J. A. O'Donoghue, S. Ruan, S. K. Lyashchenko, J. A. Carrasquillo, G. Heller, D. F. Martinez, S. M. Cheal, J. S. Lewis, M. Fleicher, J. S. Keppler, R. E. Reiter, A. M. Wu, W. A. Weber, H. I. Scher, S. M. Larson, M. J. Morris, *J. Nucl. Med.* **2016**, *57*, 1858–1864; d) D. Li, S. Cheng, S. Zou, D. Zhu, T. Zhu, P. Wang, X. Zhu, *Mol. Pharmaceutics* **2018**, *15*, 1674–1681.
[10] a) Y. Toporivska, E. Gumienna-Kontecka, *J. Inorg. Biochem.* **2019**, *198*, 110753; b) M. Savastano, C. Bazzicalupi, G. Ferraro, E. Fratini, P. Gratteri, A. Bianchi, *Molecules* **2019**, *24*, 2098; c) K. L. Summers, E. K. Sarbisheh, A. Zimmerling, J. J. H. Cotelesage, I. J. Pickering, G. N. George, E. W. Price, *Inorg. Chem.* **2020**, *59*, 17443–17452; d) R. Imura, H. Ida, I. Sasaki, N. S. Ishioka, S. Watanabe, *Molecules* **2021**, *26*, 4977; e) M. Savastano, F. Boscaro, A. Bianchi, *Molecules* **2022**, *27*, 184; f) G. Alberti, C. Zanoni, V. Losi, S. Rovertoni, L. R. Magnaghi, O. Fonquernie, S. Brandès, A. Amati, J.-C. Chambron, N. Maudoux, R. Biesuz, M. Meyer, *New J. Chem.* **2023**, *47*, 13436–13449.
[11] a) M. A. Deri, S. Ponnala, B. M. Zeglis, G. Pohl, J. J. Dannenberg, J. Lewis, L. C. Francesconi, *J. Med. Chem.* **2014**, *57*, 4849–4860; b) F. Guérard, Y. S. Lee, M. W. Brechbiel, *Chem. Eur. J.* **2014**, *20*, 5584–5591; c) M. Patra, A. Bauman, C. Mari, C. A. Fischer, O. Blacque, D. Häussinger, G. Gasser, T. L. Mindt, *Chem. Commun.* **2014**, *50*, 11523–11525; d) D. N. Pandya, S. Pailloux, D. Tatum, D. Magda, T. J. Wadas, *Chem. Commun.* **2015**, *51*, 2301–2303; e) M. A. Deri, S. Ponnala, P. Kozlowski, B. P. Burton-Pye, H. T. Cicek, C. Hu, J. S. Lewis, L. C. Francesconi, *Bioconjugate Chem.* **2015**, *26*, 2579–2591; f) E. Boros, J. P. Holland, N. Kenton, N. Rotile, P. Caravan, *ChemPlusChem* **2016**, *81*, 274–281; g) U. Seibold, B. Wängler, C. Wängler, *ChemMedChem* **2017**, *12*, 1555–1571; h) L. Allott, C. Da Pieve, J. Meyers, T. Spinks, D. M. Ciobota, G. Kramer-Marek, G. Smith, *Chem. Commun.* **2017**, *53*, 8529–8532; i) D. J. Vugts, C. Klaver, C. Sewing, A. J. Poot, K. Adamzek, S. Huegli, C. Mari, G. W. M. Visser, I. E. Valverde, G. Gasser, T. L. Mindt, G. A. M. S. van Dongen, *Eur. J. Nucl. Med. Mol. Imaging* **2017**, *44*, 286–295; j) N. B. Bhatt, D. N. Pandya, T. J. Wadas, *Molecules* **2018**, *23*, 638; k) C. Buchwalder, M. de G Jaraquemada-Peláez, J. Rousseau, H. Merkens, C. Rodríguez-Rodríguez, C. Orvig, F. Bénard, P. Schaffer, K. Saatchi, U. O. Häfeli, *Inorg. Chem.* **2019**, *58*, 14667–14681; l) D. N. Pandya, K. E. Henry, C. S. Day, S. A. Graves, V. L. Nagle, T. R. Dilling, A. Sinha, B. M. Ehrmann, N. B. Bhatt, Y. Menda, J. S. Lewis, T. J. Wadas, *Inorg. Chem.* **2020**, *59*, 17473–17487; m) E. K. Sarbisheh, A. K. Salih, S. J. Raheem, J. S. Lewis, E. W. Price, *Inorg. Chem.* **2020**, *59*, 11715–11727; n) A. H. Alnahwi, S. Ait-Mohand, V. Dumulon-Perreault, Y. Dory, B. Guérin, *ACS Omega* **2020**, *5*, 10731–10739; o) M. Chomet, M. Schreurs, M. Bolijn, M. Verlaan, W. Beiano, K. Brown, A. J. Poot, A. D. Windhorst, H. Gill, J. Marik, S. Williams, J. Cowell, G. Gasser, T. L. Mindt, G. A. M. S. van Dongen, D. Vugts, *Eur. J. Nucl. Med. Mol. Imaging* **2021**, *48*, 694–707; p) I. V. J. Feiner, M. Brandt, J. Cowell, T. Demuth, D. Vugts, G. Gasser, T. L. Mindt, *Cancers* **2021**, *13*, 4466; q) S. E. Rudd, J. K. Van Zuylekom, A. Raicevic, L. A. Pearce, C. Cullinane, C. C. Williams, T. E. Adams, R. J. Hicks, P. S. Donnely, *Chem. Sci.* **2021**, *12*, 9004–9016; r) C. S. Kang, S. Zhang, H. Wang, Y. Liu, S. Ren, Y. Chen, J. Li, N. Bandara, A. Y. Rogachev, B. E. Rogers, H.-S. Chong, *ACS Omega* **2022**, *7*, 37229–37236; s) A. K. Salih, S. J. Raheem, M. D. Garcia, W. K. Ahiahonu, E. W. Price, *Inorg. Chem.* **2022**, *61*, 20964–20976; t) H. Damerow, X. Cheng, V. von Kiedrowski, R. Schirrmacher, B. Wängler, G. Fricker, C. Wängler, *Pharmaceutica* **2022**, *14*, 2114; u) A. K. Salih, M. Dominguez-Garcia, S. J. Raheem, W. K. Ahiahonu, E. W. Price, *Inorg. Chem.* **2023**, *62*, 20806–20819.
[12] a) S. J. Rodgers, K. N. Raymond, *J. Med. Chem.* **1983**, *26*, 439–442; b) D. L. White, P. W. Durbin, N. Jeung, K. N. Raymond, *J. Med. Chem.* **1988**, *31*, 11–18.
[13] D. W. Whisenhunt, M. P. Neu, Z. Hou, J. Xu, D. C. Hoffman, K. N. Raymond, *Inorg. Chem.* **1996**, *35*, 4128–4136.
[14] J. P. Holland, *Inorg. Chem.* **2020**, *59*, 2070–2082.
[15] a) R. Raavé, G. Sandker, P. Adumeau, C. Borch Jacobsen, F. Mangin, M. Meyer, M. Moreau, C. Bernhard, L. Da Costa, A. Dubois, V. Goncalves, M. Gustafsson, M. Rijpkema, O. Boerman, J.-C. Chambron, S. Heskamp, F. Denat, *Eur. J. Nucl. Med. Mol. Imaging* **2019**, *46*, 1966–1977; b) D. S. Abou, M. Longtine, A. Fears, N. Benabdallah, R. Unnerstall, H. Johnston, K. Shim, A. Hasson, H. Zhang, D. Ulmert, F. Mangin, S. Ozen, L. Raibaut, S. Brandès, M. Meyer, J.-C. Chambron, D. S. Tatum, D. Magda, R. L. Wahl, D. L. J. Thorek, *J. Nucl. Med.* **2023**, *64*, 1062–1068.
[16] P. Jewula, J.-C. Berthet, J.-C. Chambron, Y. Rousselin, P. Thuéry, M. Meyer, *Eur. J. Inorg. Chem.* **2015**, 1529–1541.
[17] a) P. Jewula, J.-C. Chambron, M.-J. Penouilh, Y. Rousselin, M. Meyer, *RSC Adv.* **2014**, *4*, 22743–22754; b) P. Jewula, M. Grandmougin, M. Choppin, A. M. C. Tivelli, A. Amati, Y. Rousselin, L. Karmazin, J.-C. Chambron, M. Meyer, *Eur. J. Inorg. Chem.* **2023**, *26*, e202300038.
[18] a) G. J. Sharman, D. H. Williams, D. F. Ewing, C. Ratledge, *Chem. Biol.* **1995**, *2*, 553–561; b) S. Kodani, M. Ohnishi-Kameyama, M. Yoshida, K. Ochi, *Eur. J. Org. Chem.* **2011**, 3191–3196; c) Q. Wu, R. W. Deering, G. Zhang, B. Wang, X. Li, J. Sun, J. Chen, H. Zhang, D. C. Rowley, H. Wang, *Mar. Drugs* **2018**, *16*, 1–9.
[19] S. Brandès, A. Sornosa-Ten, Y. Rousselin, M. Lagrelette, C. Stern, A. Moncomble, J.-P. Cornard, M. Meyer, *J. Inorg. Biochem.* **2015**, *151*, 164–175.
[20] Of course, without taking into consideration the multiple isomers due to the different arrangements of the chelator around Zr^{4+}, as shown by the DFT calculations.
[21] Y. Liu, H. K. Jacobs, A. S. Gopalan, *Tetrahedron* **2011**, *67*, 2206–2214.
[22] J. Liu, D. Obando, L. G. Schipanski, L. K. Groebler, P. K. Witting, D. S. Kalinowski, D. R. Richardson, R. Codd, *J. Med. Chem.* **2010**, *53*, 1370–1382.
[23] D. A. Case, T. A. Darden, T. E. Cheatham, III, C. L. Simmerling, J. Wang, R. E. Duke, R. Luo, R. C. Walker, W. Zhang, K. M. Merz, B. Roberts, S. Hayik, A. Roitberg, G. Seabra, J. Swails, A. W. Götz, I. Kolossváry, K. F. Wong, F. Paesani, J. Vanicek, R. M. Wolf, J. Liu, X. Wu, S. R. Brozell, T. Steinbrecher, H. Gohlke, Q. Cai, X. Ye, J. Wang, M.-J. Hsieh, G. Cui, D. R. Roe, D. H. Mathews, M. G. Seetin, R. Salomon-Ferrer, C. Sagui, V. Babin, T. Luchko, S. Gusarov, A. Kovalenko, P. A. Kollman, AMBER 12, University of California, San Francisco, CA, 2012.
[24] M. J. Frisch, G. W. Trucks, H. B. Schlegel, G. E. Scuseria, M. A. Robb, J. R. Cheeseman, G. Scalmani, V. Barone, B. Mennucci, G. A. Petersson, H. Nakatsuji, M. Caricato, X. Li, H. P. Hratchian, A. F. Izmaylov, J. Bloino, G. Zheng, J. L. Sonnenberg, M. Hada, M. Ehara, K. Toyota, R. Fukuda, J. Hasegawa, M. Ishida, T. Nakajima, Y. Honda, O. Kitao, H. Nakai, T. Vreven, J. A. Montgomery, J. E. Peralta, F. Ogliaro, M. Bearpark, J. J. Heyd, E. Brothers, K. N. Kudin, V. N. Staroverov, T. Keith, R. Kobayashi, J. Normand, K. Raghavachari, A. Rendell, J. C. Burant, S. S. Iyengar, J. Tomasi, M. Cossi, N. Rega, J. M. Millam, M. Klene, J. E. Knox, J. B. Cross, V. Bakken, C. Adamo, J. Jaramillo, R. Gomperts, R. E. Stratmann, O. Yazyev, A. J. Austin, R. Cammi, C. Pomelli, J. W. Ochterski, R. L. Martin, K. Morokuma, V. G. Zakrzewski, G. A. Voth, P. Salvador, J. J. Dannenberg, S. Dapprich, A. D. Daniels, O. Farkas, J. B. Foresman, J. V. Ortiz, J. Cioslowski, D. J. Fox, Gaussian, Inc., Wallingford CT, 2013.
[25] P. J. Hay, W. R. Wadt, *J. Chem. Phys.* **1985**, *82*, 270–283.
[26] J. K. Burdett, R. Hoffmann, R. C. Fay, *Inorg. Chem.* **1978**, *17*, 2553–2568.
[27] D. Casanova, M. Llunell, P. Alemany, S. Alvarez, *Chem. Eur. J.* **2005**, *11*, 1479–1494.
[28] H. Shan, W. K. Wilson, E. Kamaric, *Org. Lett.* **2020**, *22*, 1714–1719.
[29] C. H. Görbitz, *Acta Crystallogr.* **1989**, *B45*, 390–395.

Manuscript received: January 23, 2024
Revised manuscript received: March 18, 2024
Version of record online: ■■, ■■

RESEARCH ARTICLE

The solution structure of the Zr(IV) complex of a linear chiral tetrahydroxamate chelator was investigated by comparing NMR and DFT computation data. The complex was obtained in the form of two diastereomers in 77 : 23 ratio in methanol. The 44 lowest energy structures, ranging between 0 and 21.5 kJ mol^{-1}, were examined in detail and the structures of the most probable ones discussed.

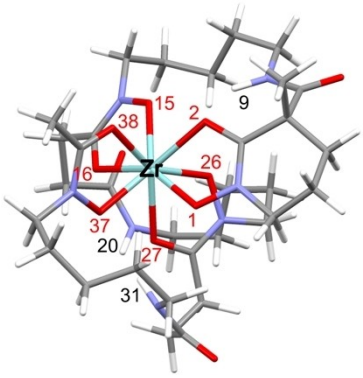

Dr. F. Mangin, Dr. O. Fonquernie, Dr. P. Jewula, Dr. S. Brandès, M.-J. Penouilh, Dr. Q. Bonnin, Dr. B. Vincent, Prof. Dr. E. Espinosa, Dr. E. Aubert, Dr. M. Meyer*, Dr. J.-C. Chambron**

1 – 14

Combining Desferriferrioxamine B and 1-Hydroxy-2-Piperidone ((PIPO)H) to Chelate Zirconium. Solution Structure of a Model Complex of the [^{89}Zr]Zr–DFOcyclo*–mAb Radioimmunoconjugate